ADVANCED FUNCTIONAL MATERIALS
www.afm-journal.de

Tunable Infrared Emissivity Using Laser-Sintered Liquid Metal Nanoparticle Films

Sooik Im, Ethan Frey, Do Hyeon Kim, Se-Yeon Heo, Young Min Song, Man Hou Vong, Sina Jamalzadegan, Qingshan Wei, Amanda A. Gregg, Omar Khatib, Willie J. Padilla, Jan Genzer, and Michael D. Dickey**

This paper describes laser exposure to tune the infrared (IR) emissivity of a film of eutectic gallium indium (EGaIn) particles. EGaIn – a liquid metal at room temperature – forms a native oxide that keeps particles of the metal from spontaneously percolating. Photothermal energy from a CO_2 laser percolates the particles into a conductive network. Here, it also causes a decrease in the IR emissivity of the film of particles from 0.4 to 0.24 over the range of 7.5–13 µm wavelength (measured by an IR camera) with the increase of laser fluence from 1.4 to 1.9 J cm^{-2}. The particles percolate most prominently at the bottom of the film, and thus, the apparent surface roughness does not change with laser exposure. This finding suggests the decrease in emissivity is not due to changes in the film's topography. Instead, the change in IR emissivity is attributed to a loss of the surface plasmonic resonance effect of EGaIn particles in the IR range after the sintering, which is confirmed by optical simulations. As a demonstration, it is shown that the ability to change the emissivity makes it possible to encrypt messages and camouflage laser-processed patterns.

1. Introduction

Control of thermal radiation from objects has received extensive attention due to its importance for selective emission of thermal energy for thermophotovoltaics,[1,2] radiative cooling of surfaces for thermal management,[3,4] and camouflaging of objects in the infrared (IR) range for disguising thermal signals.[5–7] According to the Stefan–Boltzmann law, thermal radiation from objects is proportional to the temperature (to the fourth power) and emissivity of the surface. Without changing the temperature, thermal radiation can only be controlled by surfaces with tunable emissivities, such as phase-change materials,[8,9] metamaterials,[10] dielectric materials,[11] and metals.[7,12,13] We focus here on metal coatings.

Metals have high reflectivity of IR light and thus have low emissivity according to Kirchhoff's law of radiation. Consequently, flat metal coatings are typically used to achieve near-zero IR emissivity (i.e., high IR reflectivity), particularly in the mid-IR range.[7,14] Metals generally have static optical properties. Yet, the thermal emission of metal-coated surfaces can be altered by generating cracks from stretching thin metal films to expose underlying, non-metallic substrates with high emissivity.[15–17] It can also be changed by tuning the surface topography of the film to induce the surface plasmonic resonance (SPR) effect[18] or by creating metal nanoparticles.[19,20] Thus, adjusting the IR emissivity of solid metals is typically done by changing the shape or topography of the metal. Yet it is challenging to change the shape of solids "on demand" because metals are rigid and stiff. Thus, we sought to investigate liquid metals (EGaIn, eutectic gallium indium) because of the possibility of changing the emissivity dynamically. Previously, the effective optical properties of liquid metals across other parts of the spectrum have been changed dynamically by, for example, using electrochemistry to modulate the surface roughness via electrochemical oxidation,[21] by using deformable meta-surfaces that alter the geometry of resonator structures composed of liquid metal,[22] and by using dynamic corrugated surfaces to create switchable diffraction gratings.[23] However, we found no reports of tuning the emissivity of liquid metal structures.

The optical properties of EGaIn, which have been reviewed recently,[24] have typical metallic properties. EGaIn is highly reflective in the visible range and possesses Drude-like behavior, showing the typical characteristic of metals.[25,26] Thus, bulk

S. Im, E. Frey, M. H. Vong, S. Jamalzadegan, Q. Wei, J. Genzer, M. D. Dickey
Department of Chemical and Biomolecular Engineering
North Carolina State University
Raleigh, NC, USA
E-mail: jgenzer@ncsu.edu; mddickey@ncsu.edu
D. H. Kim, S.-Y. Heo, Y. M. Song
School of Electrical Engineering and Computer Science
Gwangju Institute of Science and Technology
Gwangju, Republic of Korea
A. A. Gregg, O. Khatib, W. J. Padilla
Electrical and Computer Engineering
Duke University
Durham, NC, USA

The ORCID identification number(s) for the author(s) of this article can be found under https://doi.org/10.1002/adfm.202422453

DOI: 10.1002/adfm.202422453

EGaIn is naturally a low emissivity material, but the emissivity increases by casting films of EGaIn particles.

Yet, as we report here, the IR emissivity of films of EGaIn particles decreases after laser exposure. We discovered this behavior using an IR camera to compare the appearance of laser-exposed and pristine films resting on a hot plate. There are several possible explanations for the decrease in emissivity with laser exposure. This paper aims to explore these reasons to narrow down and ultimately identify the mechanism responsible for changes in emissivity: sub-surface sintering of the particles. In addition to exploring the mechanism, we demonstrate pattern encryption in the film by local laser exposure. The patterns are invisible to the naked eye but can be seen using an IR camera due to differences in IR emissivity between exposed and unexposed areas.

2. Results & Discussion

To create the films, EGaIn particles with an average diameter of ≈240 nm were produced by probe-sonication in isopropanol (IPA) for 10 min (Figure S1, Supporting Information) and drop-cast onto a glass slide (**Figure 1**). Additional details of the processing can be found in the methods section. EGaIn forms a ≈3 nm-thick native oxide layer, even at a ppm oxygen concentration level.[27,28] The oxide layer is essential because it keeps the particles from merging back together during processing.[29,30] Exposure of the film to a common CO_2 laser (10.6 µm wavelength) provides photothermal energy to rupture EGaIn particles due to a thermal expansion mismatch between core EGaIn and the outer oxide layer.[30–33] Particles percolate after the laser-sintering (Figure 1a,b). This process decreases the apparent temperature captured by the IR camera, demonstrating suppression of IR radiation from the surface (Figure 1c). Henceforth, we use the word "sinter" rather than "percolate" to describe the particle morphology to be consistent with the literature even though the particles do not form a dense film that one might associate with the word "sinter."

Varying the laser power tunes the IR emissivity from the film of particles. Yet, it does so without changing the apparent surface roughness, as evident from the top-view scanning electron microscopy (SEM) images in Figure 1 and as discussed in more detail herein. This surprising result led us to investigate the mechanisms that could cause such a change.

2.1. Tunable IR Emissivity

Increasing laser fluence decreased the apparent temperature from a film of EGaIn particles, as reported in **Figures 2**a and S2 (Supporting Information). An IR camera imaged the surface to detect apparent temperature while resting the sample on a hot plate. The physical temperature of the surface of the hotplate was ≈100 °C. The apparent temperature of the unsintered area was ≈90 °C because of the low IR emission of the film of particles (Figure 2a). To our surprise, the apparent temperature of the laser-sintered areas was even lower (≈60–70 °C) and decreased with higher laser fluence. The IR emissivity was estimated based on the apparent temperatures of the film measured by an IR camera (Figure 2b). We measured IR emissivity at 100 °C with the IR camera because noticeable changes in IR emissivity are observed over 80 °C (Figure S3, Supporting Information). Emissivity is a material property, whereas emission depends on emissivity and surface temperature. As a control experiment, we examined the IR emissivity of the film of particles on different substrates (glass versus Si wafer, Figure S4, Supporting Information). The results indicate a negligible difference in IR emissivity, suggesting that the IR emission originates solely from the film of the particles, not the substrate. Also, IR emissivity was measured using a customized IR microscope and Fourier transform infrared (FT-IR) at different wavelengths (3–15 µm) at 200 °C (Figure S5, Supporting Information). A detailed description of the equipment is provided in the Method section. The films' average IR emissivity values are higher than those estimated indirectly from the images from the IR camera. This difference could be due to the smaller minimum spot size (100 µm diameter) of the IR microscope compared to that of the IR camera (1.27 mm).[34] However, the general trend of change in IR emissivity was the same: IR emissivity decreases with increasing laser fluences. We heated the films to 100 °C to obtain thermal images with the IR camera and up to 200 °C to measure IR emissivity with different wavelengths. These temperatures are known not to cause thermal sintering or oxidation. Previous literature reported thermal sintering and oxidation occurring at 500 and 300 °C, respectively.[31]

We speculated that three parameters might affect the emissivity after the laser-sintering: 1) surface roughness, 2) changes to the oxide layer, or 3) changes to plasmon resonance resulting from sintering. We explore these parameters herein and show that plasmon resonance is the dominant mechanism that changes the emissivity.

Rough metal surfaces can increase emissivity due to the excitation of plasmon polaritons.[35] For example, liquid metal films with different particle sizes demonstrate this principle. Films created using particles formed by bath sonication (rather than probe sonication) had relatively larger average particle sizes (≈1 µm). These larger particles resulted in approximately a twofold increase in surface roughness, enhancing IR emission relative to the films created using smaller particles through probe sonication (Figure S1, Supporting Information) without laser processing. This result verifies the general importance of surface roughness on emissivity. For consistency, a probe sonicator was used to produce EGaIn particles for the rest of this study to ensure the films contained similar-sized particles and, thus, surface roughness.

Exposing films of liquid metal particles to the laser decreases emissivity. Still, it barely changes the area roughness (average arithmetic mean height S_a and root-mean-square height S_q) as measured by confocal microscopy (Figure 2b). Compared with previous studies of roughened metal surfaces,[35,36] the small variation for roughness ($\Delta S_{a,q} < 0.1$ µm) is negligible compared to what is needed to change the emissivity. SEM and atomic force microscopy (AFM) of the film also confirmed insignificant changes in roughness after the laser sintering (Figure 1a,b; Figure S6, Supporting Information). Yet, there are some minor changes to the surface. For example, in Figure 1b, some of the particles show evidence of excess oxide "skin," which has been shown previously to form due to the sudden, yet temporary, increase in surface area with thermal expansion during laser exposure. In subsequent sections, we discuss the role of oxide and

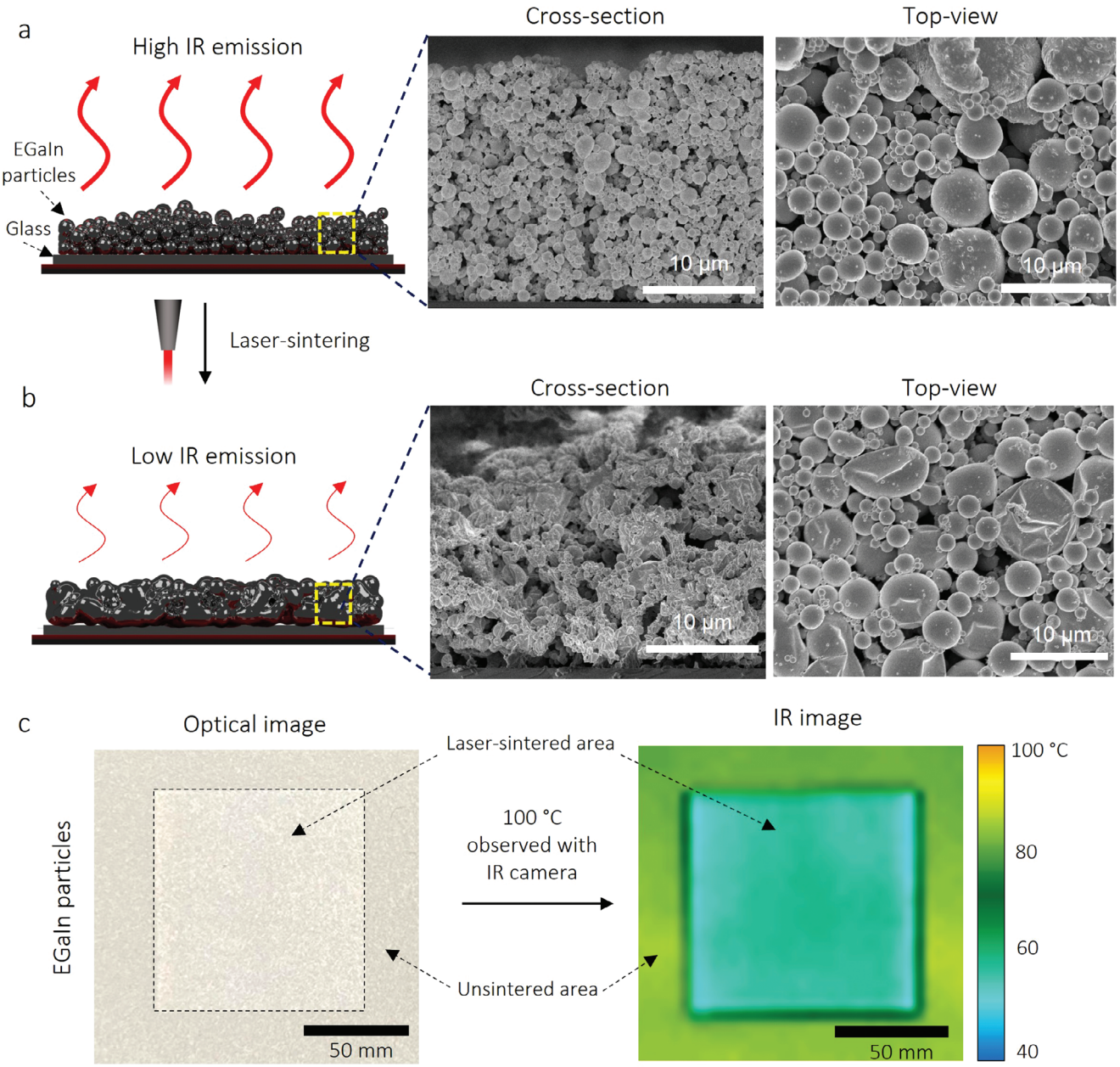

Figure 1. IR emission control by exposing a surface to a laser. a,b) Schematics (left) and cross-sectional (middle) and top (right) morphologies of EGaIn particles (a) before and b) after laser-sintering, which shows how the particles percolate to form a conductive network, yet do so without changing the top-down surface topography. c) Optical (left) and IR thermal (right) images of a laser-sintered square pattern of EGaIn particles. The laser-sintered region is similar to the unsintered area, yet the emissivity decreases significantly based on the IR image. The sample was placed onto a hot plate at 100 °C for the IR image. EGaIn particles were produced by probe sonication for 10 min. The laser fluence was 1.87 J cm^{-2}.

note here that the surface roughness does not appear to change significantly with laser exposure over the range of intensities studied here.

Having ruled out surface roughness as a primary factor in explaining changes arising from laser sintering, we explored other changes to the film that result from laser exposure and could alter the film's IR emissivity. We speculated that the oxide on the metal – which is composed primarily of amorphous Ga_2O_3 – thickens during the photothermal laser exposure. Although we could not find literature reports on the transparency of amorphous Ga_2O_3, prior studies suggest crystalline Ga_2O_3 has high IR transparency (>80% at a thickness of 560 nm).[37] Thus, we do not expect changes to the oxide to affect the IR emissivity. Nevertheless, we explored whether the oxide thickens from laser exposure to test if it might explain the change emissivity.

The oxide layer before and after the laser-sintering was analyzed with X-ray photoelectron spectroscopy (XPS), scanning transmission electron microscopy (S/TEM), and time of

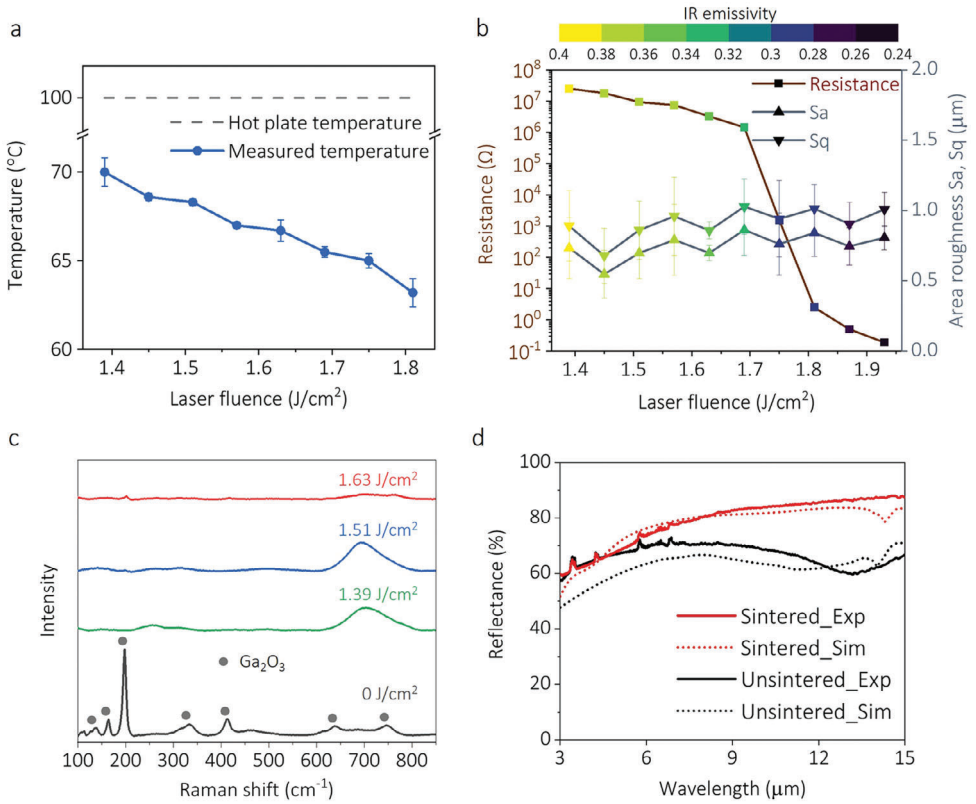

Figure 2. Tunable IR emissivity. a) The measured temperature of films of liquid metal (EGaIn) particles on a hot plate at 100 °C after exposure to different laser fluences. b) Resistance and area roughness (S_a and S_q) with different laser fluences. IR emissivity was obtained from the difference in real and apparent temperature of laser-sintered EGaIn particles. The gradient color of the data points from yellow to purple shows the different IR emissivity. c) Raman spectrum of EGaIn particles layers before and after the laser-sintering. d) Experimental and numerical simulation of total reflectance of EGaIn particles in the wavelength of 3–15 μm before and after the laser-sintering. The laser fluence was 1.75 J cm^{-2}.

flight-secondary ions mass spectrometer (TOF-SIMS) (Figures S7–S9, Supporting Information). These analyses suggest an increase in oxidation of the metal after the laser-sintering. While we tried to image the oxidation thickness directly using S/TEM, it was difficult to separate individual particles from the sintered region of the film (Figure S8, Supporting Information). To isolate the particles, we sonicated the film to detach the particles from the substrate. However, this aggressive physical process could affect the morphology of the particles. It should also release the weakest bound particles in the film, which may have not fully sintered and, thus, may not be representative. We also observed differences in TOF-SIMS of films with and without laser exposure, suggesting increased oxidation (Figure S9, Supporting Information). However, interpreting such results is also challenging since the substrate contains liquid. Thus, the sample surface can flow during the Cs ions sputtering process used during TOF-SIMS measurements. The most direct evidence of increased oxidation is from XPS. From Ga 3d survey, the relative intensity ratios of gallium oxide to gallium metal increase from 1.37 to 1.84 after the laser-sintering (Figure S7a, Supporting Information). We note, however, that XPS is a surface-sensitive technique that only probes the topmost surface of the particle film.

To investigate the impact of oxidation on IR reflectance, we conducted optical simulations using rigorous coupled-wave analysis (RCWA). Additional details of the simulation appear in the methods section. In Figure S10 (Supporting Information), the RCWA calculation shows negligible change in average IR reflectance in the wavelength range of 3–15 μm with increasing oxidation (oxide thickness from 0 to 20 nm), suggesting that it did not affect IR emissivity. This could be due to the low absorptivity of Ga_2O_3 (assuming the optical properties reported for crystalline Ga_2O_3[38,39]) and the relatively small increase in oxide thickness. Thus, we hypothesized that the changes in the geometry of the liquid metal arising from the particle sintering decreases the film IR emissivity. Sintering causes the film to become more bulk-like, and bulk metal films have lower emissivity relative to a film of particles.

One way to determine if the particles sinter is to measure the electrical resistance. Before laser exposure, the films are resistive. Figure 2b shows that electrical resistance (in-plane) and IR emissivity from the surface decreases with increasing laser fluence. The cross-sectional SEM images with different laser fluences also confirm increased percolation between particles at higher laser fluences (Figure S11, Supporting Information). We report one more source of indirect evidence for sintering, particularly its effect on the interaction of light with the film. Since the thickness of gallium oxide is very thin, it is impossible to detect Raman scattering from the surface of a smooth, bulk liquid metal film. However, due to enhanced Raman scattering between the particles, gallium oxide peaks were detected in films of unsintered

particles (black data, Figure 2c).[40] After laser-sintering, gallium oxide peaks were no longer detected despite the increase in oxidation. Raman scattering is detected by a laser with a wavelength of 532 nm; thus, the observation after the Raman shift (534.85–558.75 nm) is not in the IR region. Nevertheless, the decrease in signal intensity after sintering indicates that the film becomes more bulk-like.

To better understand why sintering may alter emissivity, we measured the total IR reflectance of films of EGaIn particles in the range of IR wavelengths of 3–15 μm (Figure 2d) before and after laser-sintering. Over this range, the IR reflectance increases after the laser-sintering, indicating reduced emissivity. This trend is the same as that observed by the IR camera in Figure 2a. At ≈12 μm wavelength, the unsintered EGaIn particles show a U-shaped dip in reflectance. This reflectance dip is consistent with the previously reported localized surface plasmon resonance (LSPR) effect in the IR region, induced by particle configurations.[41–43] Laser exposure weakens this effect by sintering the EGaIn particles and making the film less particle-like. Consequently, the IR emissivity decreases.

RCWA simulation (dotted lines) further confirms a similar increase in total reflectance (i.e., decrease in emissivity) after the laser-sintering. In these simulations, we utilized models incorporating particle structures with random sizes and distributions (Figure S12, Supporting Information) to represent the morphology captured by SEM images (Figure S1, Supporting Information). Considering that 1) an SEM image only provides a cross-sectional view of particle size, distribution, and spacing, and 2) such a non-periodic arrangement is difficult to mimic in a model, it is expected that there will be slight disparities between simulated and experimental reflectance, especially in unsintered particles. Despite these differences, both simulated and measured results show that the unsintered structure exhibits higher emissivity due to stronger LSPR effects than the sintered structure.

To explore the effect of particle size and spacing on LSPR, we have conducted simulations varying these two parameters using models based on a single particle and periodic arrays (Figures S13 and S14, Supporting Information). The results show that as particles get larger – such as that experienced by sintering– the reflectance dips weaken and shift toward longer wavelength (Figure S13, Supporting Information). The modeling also provides the electric field distribution around a single EGaIn particle (Figure S14, Supporting Information). The electric field is confined next to EGaIn particles (red regions), showing LSPR. The LSPR effect disappears, and the particles start to scatter when the particle size increases to 3 μm or the wavelength of incident light increases to 12.6 μm. Combining these results with the experimental observations, we reason that LSPR causes a dip in IR reflectance from a wavelength range of 6–15 μm (Figure 2d). However, when the particles sinter, that dip effectively disappears due to the bulk-like configuration. Thus, the most self-consistent explanation for reduced IR emissivity is that sintered layers result in a loss of the LSPR effect.

Another optical simulation was conducted using the finite-difference time-domain (FDTD) method to simulate the absorption spectra of a periodic 3D EGaIn nanoparticle assembly to explore possible trends as a function of particle sintering and validate previous simulations. The model explores what happens to light as the particles get closer together and ultimately overlap (touch) in the array. Both RCWA and FDTD simulations solve Maxwell's equations for optical modeling. While RCWA is a semi-analytical method with staircase approximation for curved features with trapezoid grating, FDTD discretizes space into confined cubic cells to solve the electromagnetic equations fully numerically. The simulation details appear in the methods section and Figures S15–S17, Supporting Information. According to the model, the power cross-sections of absorption (i.e., the total absorbed power divided by the power of the illumination source per unit area) decreased after sintering. (Figure S17, Supporting Information). A decrease in power cross-section (a measure of absorption) implies that the reflectance increases (and emissivity decreases) with sintering, consistent with experimental observation. The exact location of the peaks (LSPR) differs from our experiments, likely due to the assumption of a periodic lattice of uniform particles. However, the general trends agree with the observations of an increase in reflectance in the IR range with sintering. These results suggest that the connection of individual particles by sintering could lead to a loss of the LSPR of the film of EGaIn particles in the IR range, consistent with the RCWA simulation results.

Thus, by process of elimination, this study suggests that the decrease in emissivity from laser sintering is not from changes in surface roughness or increased oxidation. Instead, it indicates that the decrease in emissivity is due to particles sintering. The sintering makes the particles more "bulk-like" and diminishes the LSPR effect.

2.2. Encryption

Tunable IR emission from films of laser-sintered EGaIn particles was employed to encrypt letters and patterns within a film of particles (**Figure 3**). Figure 3a demonstrates the IR encryption of the letters "F" and "I" within the letter "E" by tuning the laser fluence on the film of EGaIn particles. The entire letter "E" was exposed to the laser, but only part (F and I) was exposed to higher laser fluences. The EGaIn particles exposed to the laser become optically brighter at visible wavelengths; thus, the letter "E" is apparent in film optical photographs. When the film was observed with the IR camera, the encrypted letters "F" or "I" appeared due to the more intense laser exposure in those regions.

As another demonstration, the letters "NCSU" were encrypted by tuning laser fluence (Figure 3b). We used a similar approach as in Figure 3a, using a higher laser power of 1.75 J cm^{-2} to pattern the letters and a lower laser power of 1.39 J cm^{-2} to sinter the particles in the film surrounding the letters, forming four laser-sintered rectangular regions. The entire film was exposed to a low-intensity laser; thus, the letters cannot be seen by the eye. The letters "NCSU" exposed to higher laser fluence are only visible by IR thermal imaging (Figure 3c). We also processed the optical images with various pseudo colors to see any visual changes in the images (Figure S18, Supporting Information). The boundary between the logo and surrounding areas becomes more apparent, but still, it's difficult to identify the pattern. Video S1 (Supporting Information) demonstrates various light conditions, angles, and distances between the sample and the camera, showing that the pattern is hardly recognized in the visible wavelengths but can be seen with IR thermal imaging. The slight increase in the

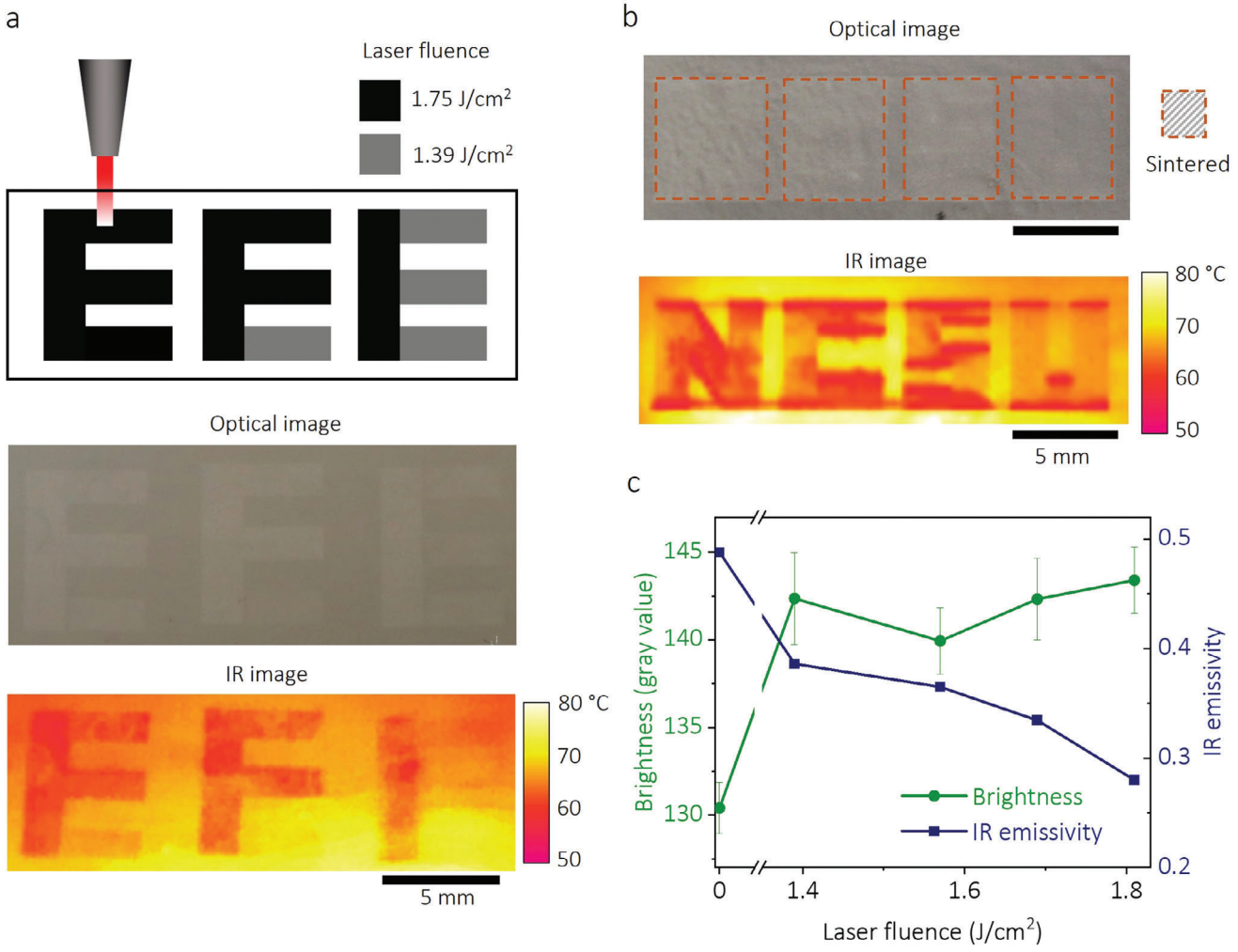

Figure 3. Encryption. a) Schematic diagram of laser patterns to encrypt the letters "E", "F", and "I" using different laser powers. An optical image (top) of the letter "E" s and how these are shown in IR thermal image (bottom). b) Optical (top) and IR image (bottom) of laser patterned EGaIn particles with the encryption of "NCSU" appearing only in the IR image. c) Gray-scale intensity (brightness) and IR emissivity of EGaIn particles with different laser fluences.

optical brightness of the film after laser exposure is due to the rise in the visible reflectance (Figure S19, Supporting Information). It has been reported that EGaIn particles also brighten after the sintering process with non-IR lasers,[30,31,44] but the detailed mechanism of the brightness increase is unclear.

3. Conclusion

Laser-sintering a film of liquid metal particles changes the IR emissivity of the film. Laser-sintering does not change the surface roughness. Instead, it percolates the EGaIn particles, leading to an increase in IR reflectivity and, thus, a decrease in emissivity. The effect is most pronounced when the film percolates into a conductive film. The decline in emissivity causes surfaces to appear cooler during IR imaging than in reality. For example, a film on a 100 °C hot plate may appear 30–40 °C cooler depending on the fluence of the prior laser exposure. The unsintered EGaIn particles have a dip in reflection centered near ≈13 µm in the IR range. After sintering, this dip disappears, which is attributed to a decrease in the LSPR effect. Two optical simulations found similar trends, consistent with the role of sintering. Interestingly, surface-enhanced Raman scattering occurs in a film of unsintered particles, as demonstrated by the sharp gallium oxide peaks that are typically hard to detect on smooth films of bulk EGaIn. After the laser-sintering, these peaks disappear due to the sintering. Control of IR emissivity was used to encrypt both letters and camouflage patterns drawn by the laser. The letters or patterns were hard to identify with optical images, but they became apparent when using an IR camera. This study may broaden the application of liquid metal particles in optical applications and provides a unique way to alter the emissivity of surfaces.

4. Experimental Section

Materials: Liquid metal (75.5 wt.% Ga, 24.5 wt.% In) was purchased from the Indium Corporation. Glass slides (20 mm × 70 mm × 5 mm, VWR) were used as substrates for the EGaIn particles. Isopropanol was purchased from Fisher.

Sample Preparation: 0.2 g EGaIn in 10 ml isopropanol was probe sonicated (Q700 Probe Sonicator, Qsonica Instruments) for 10 min at 40% amplitudes in an ice bath. The solution was cast on a glass slide and kept at room temperature for 10 min to settle the particles on the substrate. The temperature was then increased to 60 °C for 1 h to fully evaporate the solvent. The thickness of the films was maintained at ≈15 µm throughout the experiments. The films were held at a constant thickness because IR emissivity decreases with increasing film thickness (Figure S20, Supporting Information).

Laser-Sintering: A 40 W CO_2 laser (VLS 3.50, Universal) with 10.6 µm wavelength was used to sinter EGaIn particles with the raster mode. Universal Laser Systems 2.0 lens was used with a focal length of 2 inch (50.8 mm) and a nominal focus spot size of 0.0005 inches (127 µm). Laser fluence was calculated by estimating actual laser powers based on a previous paper in our group[45] and measuring the time for the laser to raster 1 cm^2 area.

Characterization: Field emission scanning electron microscopy (FE-SEM) (FEI Verios 460 L) was used to observe the morphology of EGaIn particles. An IR camera (FLIR SC300-Series) with a spectral range of 7.5–13.0 µm was kept 1 m from the samples, and the IR emissivity of the IR camera was initially set to 0.95. That assumption causes the discrepancy between the samples' apparent temperatures (measured by IR camera) and the actual temperatures (measured by a hot plate and temperature probe). With the IR camera software, IR emissivity was adjusted and determined by changing the apparent temperatures to match the actual temperatures. The emissivity measurements were performed with a Bruker Hyperion infrared (IR) microscope and Vertex 80v Fourier transform infrared (FT-IR) spectrometer. The setup includes a liquid nitrogen-cooled MCT to detect emission, a 15x cassegrain objective lens, and a KBr beam splitter. The spot size of the microscope is 100 µm. EGaIn particles were laser-sintered at 5 mm × 5 mm-sized squares on glass slides. The samples were mounted to the cold plate of a Linkam LTS420 cryostat stage housed in the IR microscope, and emitted radiation was sent to the FT-IR for spectral analysis. A temperature controller was used to change the sample and reference temperatures, and carbon black was used as the reference. To obtain the emissivity of the EGaIn particle films, the emission of the sample was divided by the emission of the carbon black reference. A new reference measurement was taken prior to each measurement of the samples. Electrical measurements were carried out with an electrometer (Keithley 2400, Tektronix) with a four-point probe. Confocal laser scanning microscopy (VKx1100, Keyence) with laser profilometry 150x objective lens and atomic force microscopy (AFM) (Asylum MRP-3D, Oxford Instruments) was used to determine the roughness of EGaIn particles before and after the laser-sintering. Fourier transform-infrared (Nicolet is50, Thermo Scientific) with an integrating sphere (Pike Technologies) was used to measure the total IR reflectance of EGaIn particles. A gold-coated Si wafer was used as a reference for the reflectivity of 1. A confocal Raman microscope (Horiba XploRA PLUS) was used to detect gallium oxide on the surface of EGaIn particles. Particle size distribution of EGaIn particles was determined through dynamic light scattering (DLS, Zetasizer Nano ZSP, Malvern Instruments). For the sample preparation of DLS measurement, an IPA solution containing EGaIn particles was filtered by a 1 µm syringe filter not to block the light pathway. Due to the filtering, DLS could not detect bigger particles higher than 1 µm; the particle size distribution was also determined by image analysis (ImageJ) from top-view SEM images. X-ray photoelectron spectroscopy (XPS) (PHOIBOS 150 Analyzer) was carried out on a SPECS system with an Mg Kα source. XPS was used to determine the surface chemistry before and after the sintering. S/TEM (Talos F200X, ThermoFisher) and energy-dispersive X-ray spectroscopy (EDS) were used to image EGaIn particles before and after the laser-sintering. TOF-SIMS was used to quantify the thickness of the gallium oxide layer before and after the laser sintering. For the depth profiles, 1 keV Cs^+ with 7 nA current was used to sputter 120 µm by 120 µm area, and negative secondary ions were analyzed in the middle of 50 µm by 50 µm area using 0.4 pA Bi_3^+ ion beam. UV–vis spectrophotometer (Evolution 300, Thermo Scientific) with an integrating sphere (DRA-EV-300, Thermo Scientific) was used to measure the total reflection of EGaIn particles in the visible wavelength. The reflection was calibrated by Fluorilon 99 W (Avian Technologies) as a reference for the reflectivity of 1.

RCWA Calculation: The RCWA-based commercial software (DiffractMOD, RSoft Design Group, Synopsys) was employed to simulate the emissivity spectra for all samples. In addition, electric field distributions were simulated using this software. In all simulations, a square grid size of 0.5 nm was utilized with a large number of spatial harmonics (i.e., 10) for sufficiently stable results. Transverse magnetic (TM) mode was considered to confirm the scattering effect of EGaIn particles in the 2D simulation. Moreover, complex refractive indices were considered to obtain accurate spectral results. The used complex optical constants of EGaIn[46] and Ga_2O_3[38,39] were obtained from the literature. We designed the geometries of sintered and unsintered films using an array layout generator in software. The random function of particle position was introduced for the random distribution. By controlling the period parameter, the randomness amplitudes of distribution changed. The periods of the sintered and unsintered structures were set to 100 and 630 nm, respectively.

FDTD Simulation: The FDTD numerical simulation was run by the Ansys Lumerical software (2022 R2.1). The permittivities of EGaIn in the 400–1000 nm range reported in the literature[25] were extrapolated to the IR range of 3–15 µm using the Drude-Lorentz equations (Equations (1) and (2)):

$$\varepsilon_1(E) = 1 - \frac{E_p^2}{\left(E^2 + \gamma^2\right)} \tag{1}$$

$$\varepsilon_2(E) = 1 - \frac{E_p^2 \gamma}{E\left(E^2 + \gamma^2\right)} \tag{2}$$

where ε_1 and ε_2 represent the real and imaginary part of the permittivity, respectively. E_p and γ represent the plasma frequency and broadening parameters. Figure S12 (Supporting Information) shows the extrapolated real and imaginary parts of the permittivity of EGaIn in the 3–15 µm wavelength range. A model was created with a 3D EGaIn nanoparticle assembly containing 10 × 6 × 6 individual nanoparticles with the same nanoparticle diameter of 200 nm to mimic the experimental EGaIn nanoparticle film. Figure S13 (Supporting Information) shows the perspective view and top view of the 3D model with a reduced interparticle distance *d*, respectively. The 3D model was then illuminated with a broadband plane-wave source in the IR wavelength range (3–15 µm) in X, Y, and Z directions, respectively (Figure S13a, Supporting Information, red arrows). Each source has a polarization angle of 90° (Figure S13a, Supporting Information, black double arrows). The simulation time was set to 1000 fs at 300 K. The mesh size was set uniformly at 5 nm. A s-polarized (90° polarization angle) plane source with 3–15 µm wavelength was used to illustrate the 3D nanoparticle assembly model from X, Y, and Z directions to study the absorption response. The degree of the sintering was controlled by reducing the interparticle distance.

Supporting Information

Supporting Information is available from the Wiley Online Library or from the author.

Acknowledgements

This work was performed in part at the Analytical Instrumentation Facility (AIF) at North Carolina State University, which is supported by the State of North Carolina and the National Science Foundation (award number ECCS-2025064). This work made use of instrumentation at AIF acquired with support from the National Science Foundation (DMR-1726294). The AIF is a member of the North Carolina Research Triangle Nanotechnology Network (RTNN), a site in the National Nanotechnology Coordinated Infrastructure (NNCI).

Conflict of Interest

The authors declare no conflict of interest.

Data Availability Statement

The data that support the findings of this study are available from the corresponding author upon reasonable request.

Keywords

EGaIn, IR emissivity, IR encryption, laser-sintering, liquid metal particles

Received: November 19, 2024
Published online: December 8, 2024

[1] R. Sakakibara, V. Stelmakh, W. R. Chan, M. Ghebrebrhan, J. D. Joannopoulos, M. Soljačić, I. Čelanović, *J. Photonics Energy* **2019**, *9*, 032713.
[2] Z. Wang, D. Kortge, Z. He, J. Song, J. Zhu, C. Lee, H. Wang, P. Bermel, *Sol. Energy Mater. Sol. Cells* **2022**, *238*, 111554.
[3] A. P. Raman, M. A. Anoma, L. Zhu, E. Rephaeli, S. Fan, *Nature* **2014**, *515*, 540.
[4] B. Zhao, M. Hu, X. Ao, N. Chen, G. Pei, *Appl. Energy* **2019**, *236*, 489.
[5] S. A. Morin, R. F. Shepherd, S. W. Kwok, A. A. Stokes, A. Nemiroski, G. M. Whitesides, *Science* **2012**, *337*, 828.
[6] Y. Qu, Q. Li, L. Cai, M. Pan, P. Ghosh, K. Du, M. Qiu, *Light Sci. Appl.* **2018**, *7*, 26.
[7] M. Li, D. Liu, H. Cheng, L. Peng, M. Zu, *Sci. Adv.* **2020**, *6*, eaba3494.
[8] J. Park, J.-H. Kang, X. Liu, S. J. Maddox, K. Tang, P. C. McIntyre, S. R. Bank, M. L. Brongersma, *Sci. Adv.* **2018**, *4*, eaat3163.
[9] C. Kim, Y. Kim, M. Lee, *Adv. Mater. Technol.* **2022**, *7*, 2101349.
[10] Z. J. Coppens, J. G. Valentine, *Adv. Mater.* **2017**, *29*, 1701275.
[11] G. Bakan, S. Ayas, M. Serhatlioglu, C. Elbuken, A. Dana, *Adv. Opt. Mater.* **2018**, *6*, 1800613.
[12] T. Inoue, M. D. Zoysa, T. Asano, S. Noda, *Nat. Mater.* **2014**, *13*, 928.
[13] L. Peng, D. Liu, H. Cheng, S. Zhou, M. Zu, *Adv. Opt. Mater.* **2018**, *6*, 1801006.
[14] A. H. Sully, E. A. Brandes, R. B. Waterhouse, *Br. J. Appl. Phys.* **1952**, *3*, 97.
[15] C. Xu, G. T. Stiubianu, A. A. Gorodetsky, *Science* **2018**, *359*, 1495.
[16] E. M. Leung, M. C. Escobar, G. T. Stiubianu, S. R. Jim, A. L. Vyatskikh, Z. Feng, N. Garner, P. Patel, K. L. Naughton, M. Follador, E. Karshalev, M. D. Trexler, A. A. Gorodetsky, *Nat. Commun.* **2019**, *10*, 1947.
[17] A. Krishna, J. M. Kim, J. Leem, M. C. Wang, S. Nam, J. Lee, *Nano Lett.* **2019**, *19*, 5086.
[18] A. Kazemi Moridani, R. Zando, W. Xie, I. Howell, J. J. Watkins, J.-H. Lee, *Adv. Opt. Mater.* **2017**, *5*, 1600993.
[19] J. A. Fan, C. Wu, K. Bao, J. Bao, R. Bardhan, N. J. Halas, V. N. Manoharan, P. Nordlander, G. Shvets, F. Capasso, *Science* **2010**, *328*, 1135.
[20] N. J. Halas, S. Lal, W.-S. Chang, S. Link, P. Nordlander, *Chem. Rev.* **2011**, *111*, 3913.
[21] K. Nakakubo, H. Yoshioka, K. Morita, R. Ishimatsu, A. Kiani, H. Hallen, M. D. Dickey, Y. Oki, *Opt. Mater. Express* **2021**, *11*, 2099.
[22] J. Wang, S. Liu, Z. V. Vardeny, A. Nahata, *Opt. Express* **2012**, *20*, 2346.
[23] M. G. Mohammed, M. D. Dickey, *Sens. Actuators Phys.* **2013**, *193*, 246.
[24] P. Q. Liu, X. Miao, S. Datta, *Opt. Mater. Express* **2023**, *13*, 699.
[25] D. Morales, N. A. Stoute, Z. Yu, D. E. Aspnes, M. D. Dickey, *Appl. Phys. Lett.* **2016**, *109*, 091905.
[26] M. G. Blaber, C. J. Engel, S. R. C. Vivekchand, S. M. Lubin, T. W. Odom, G. C. Schatz, *Nano Lett.* **2012**, *12*, 5275.
[27] Z. J. Farrell, C. Tabor, *Langmuir* **2018**, *34*, 234.
[28] Y. Lin, J. Genzer, M. D. Dickey, *Adv. Sci.* **2020**, *7*, 2000192.
[29] J. N. Hohman, M. Kim, G. A. Wadsworth, H. R. Bednar, J. Jiang, M. A. LeThai, P. S. Weiss, *Nano Lett.* **2011**, *11*, 5104.
[30] Y. Lin, C. Cooper, M. Wang, J. J. Adams, J. Genzer, M. D. Dickey, *Small* **2015**, *11*, 6397.
[31] S. Liu, S. N. Reed, M. J. Higgins, M. S. Titus, R. Kramer-Bottiglio, *Nanoscale* **2019**, *11*, 17615.
[32] S. Liu, M. C. Yuen, E. L. White, J. W. Boley, B. Deng, G. J. Cheng, R. Kramer-Bottiglio, *ACS Appl. Mater. Interfaces* **2018**, *10*, 28232.
[33] B. Deng, G. J. Cheng, *Adv. Mater.* **2019**, *31*, 1807811.
[34] N. Playà-Montmany, G. J. Tattersall, *Methods Ecol. Evol.* **2021**, *12*, 828.
[35] C.-D. Wen, I. Mudawar, *Int. J. Heat Mass Transf.* **2006**, *49*, 4279.
[36] C.-D. Wen, I. Mudawar, *Int. J. Heat Mass Transf.* **2004**, *47*, 3591.
[37] A. M. Hassanien, A. A. Atta, M. M. El-Nahass, S. I. Ahmed, A. A. Shaltout, A. M. Al-Baradi, A. Alodhayb, A. M. Kamal, *Opt. Quantum Electron.* **2020**, *52*, 194.
[38] A. Paskaleva, D. Spassov, P. Terziyska, *J. Phys. Conf. Ser.* **2017**, *794*, 012017.
[39] M. Feneberg, J. Nixdorf, M. D. Neumann, N. Esser, L. Artús, R. Cuscó, T. Yamaguchi, R. Goldhahn, *Phys. Rev. Mater.* **2018**, *2*, 044601.
[40] X. Chen, Q. Chen, D. Wu, Y. Zheng, Z. Zhou, K. Zhang, W. Lv, Y. Zhao, L. Lin, D. Sun, *J. Raman Spectrosc.* **2018**, *49*, 1301.
[41] L. Martin-Monier, T. D. Gupta, W. Yan, S. Lacour, F. Sorin, *Adv. Funct. Mater.* **2020**, *31*, 2006711.
[42] X. Miao, T. S. Luk, P. Q. Liu, *Adv. Mater.* **2022**, *34*, 2107950.
[43] J. Zhu, W. Wei, B. Chen, P. Tang, X. Zhao, C. Wu, *ACS Photonics* **2024**, *11*, 1857.
[44] C. Cho, W. Shin, M. Kim, J. Bang, P. Won, S. Hong, S. H. Ko, *Small* **2022**, *18*, 2202841.
[45] K. Mondal, Y. Liu, T. Shay, J. Genzer, M. D. Dickey, *ACS Appl. Polym. Mater.* **2020**, *2*, 1848.
[46] L. R. Finkenauer, Q. Lu, I. F. Hakem, C. Majidi, M. R. Bockstaller, *Langmuir* **2017**, *33*, 9703.